

## Article

# Preparation and Photocatalytic Hydrogen Production of Pink ZnS

Shangjie Gao, Yongxin Lu, Teng Ma, Haixia Liu \* and Jie Zhang \* 

Shandong Provincial Key Laboratory of Molecular Engineering, School of Chemistry and Chemical Engineering, Qilu University of Technology (Shandong Academy of Sciences), Jinan 250353, China; 10431220335@stu.qlu.edu.cn (S.G.); 10431220336@stu.qlu.edu.cn (Y.L.); 10431231074@stu.qlu.edu.cn (T.M.)

\* Correspondence: liuhaixia@qlu.edu.cn (H.L.); zh\_jie@qlu.edu.cn (J.Z.)

**Abstract:** With the continuous growth of global energy demand and the increasingly severe environmental issues, the extensive utilization of traditional fossil fuels has led to serious energy crises and environmental pollution problems. In this study, a hydrothermal method was employed, and by adding ethanolamine and controlling different temperatures, pink zinc sulfide with zinc vacancies was synthesized. UV-Vis DRS analysis indicated that the sample exhibited significant visible light absorption characteristics within the wavelength range of 500–550 nm. The presence of zinc vacancies was confirmed through XPS. Due to the existence of zinc vacancies, the sample demonstrated excellent photocatalytic hydrogen evolution activity without the need for co-catalysts, with the optimal sample achieving a hydrogen evolution rate of  $7631.70 \mu\text{mol h}^{-1} \text{g}^{-1}$ . Zinc vacancies can provide additional active sites, enhance catalytic efficiency, and promote the separation of photogenerated electrons and holes. Furthermore, the introduction of vacancies effectively reduces the bandgap of the material, significantly broadening its visible light absorption range. This work provides a new approach for enhancing hydrogen evolution in pure ZnS and offers novel strategies for the further design of ZnS-related photocatalysts.

**Keywords:** pink ZnS; vacancy; temperature; photocatalytic hydrogen evolution



Academic Editors: Francis Verpoort, Alejandro Pérez-Larios, Mamoun Fellah and Naouel Hezil

Received: 11 April 2025

Revised: 29 April 2025

Accepted: 14 May 2025

Published: 15 May 2025

**Citation:** Gao, S.; Lu, Y.; Ma, T.; Liu, H.; Zhang, J. Preparation and Photocatalytic Hydrogen Production of Pink ZnS. *Inorganics* **2025**, *13*, 166. <https://doi.org/10.3390/inorganics13050166>

**Copyright:** © 2025 by the authors. Licensee MDPI, Basel, Switzerland. This article is an open access article distributed under the terms and conditions of the Creative Commons Attribution (CC BY) license (<https://creativecommons.org/licenses/by/4.0/>).

## 1. Introduction

As the world grapples with surging energy needs and intensifying environmental crises, the development of sustainable and clean energy solutions has become an urgent priority [1,2]. Solar energy, an inexhaustible and clean energy source, has attracted significant research attention for its conversion into chemical energy through photocatalysis, particularly for hydrogen evolution via water splitting [3,4]. In 1972, Fujishima first discovered that electrons and holes produced by titanium dioxide under the excitation of ultraviolet light can decompose water into oxygen and hydrogen. Titanium dioxide material then entered the research field of vision of researchers. Titanium dioxide material has excellent characteristics such as good light stability and non-toxicity [5–8]. However, titanium dioxide has a wide bandgap (3.2 eV), which significantly restricts its ability to fully utilize and convert visible light energy [9–11]. Consequently, researchers have begun exploring alternative semiconductor materials to replace titanium dioxide. Nevertheless, developing an ideal photocatalyst for practical applications that exhibits high activity, low cost, and long-term stability under visible light remains a significant challenge. To date, numerous efforts have been made to develop suitable semiconductor photocatalysts to obtain high activities for water splitting [12–15]. Photocatalytic hydrogen production through

water splitting using semiconductors is a promising approach that converts abundant solar energy into clean chemical energy, contributing to sustainable development [16–22].

ZnS, as an important wide-bandgap II-VI semiconductor material, has found extensive applications in CO<sub>2</sub> photoreduction [23,24], organic pollutant degradation [25,26], and photocatalytic water splitting for hydrogen production [27,28] due to its unique properties [29]. However, its relatively large bandgap significantly limits sunlight utilization efficiency [28,30]. A good hydrogen evolution photocatalyst should not only have a wide solar spectrum absorption range and a suitable band edge but also have a high carrier separation efficiency and a rich reaction site. Therefore, many attempts have been made to improve its catalytic performance. As is common sense, the nature of materials determines their mechanisms and performances in reactions, including photocatalytic hydrogen evolution reactions (HERs). For instance, defect states [31–33], crystalline phases [34,35], and exposed facets [36–38] of semiconductor photocatalysts can regulate the light response for robust charge generation, dominate the kinetics of charge transfer for effective charge separation, and organize active sites or facets for resultful charge utilization. For example, in photocatalysts, defects can serve as active sites for trapping light-generating carriers, thus promoting catalytic performance [13]. On the other hand, defects may also act as recombination centers, thus hindering photocatalytic activity [39]. This approach enables atomic-scale regulation and the construction of active sites on the photocatalyst surface. Extensive research has demonstrated that vacancies not only increase the number of active sites in photocatalytic reactions, facilitating the adsorption of water molecules and promoting their dissociation into hydrogen and oxygen, but also alter the local electronic structure at the vacancy sites, reducing the reaction energy barrier and thereby enhancing hydrogen evolution efficiency [13]. Various procedures have been developed to fabricate ZnS nanostructures such as electrochemical deposition [40], microemulsion [41], solvothermal [42], sol–gel [43], co-precipitation [44], combustion synthesis [45], pyrolysis [46], hydrothermal [47], laser ablation [48], and vapor deposition [49]. The hydrothermal method is versatile, able to control the process, productive, adjustable, does not need calcination and milling operations, has low contamination, and is cost-effective [50–52]. In addition, the hydrothermal/solvothermal approach allows for the precise control of the vacancy concentration and distribution through reaction conditions, making it applicable to a wide range of materials and relatively straightforward procedures [53]. Xu et al. [54] prepared PVP and excess thiourea using the hydrothermal method and synthesized ZnS hollow nanospheres with uniform sizes and good dispersion. Their results showed that hollow nanospheres with a small particle size and good dispersion have a good photocatalytic effect. Liang et al. [55] synthesized zinc sulfide globose titanium dioxide flowers with different hydrothermal synthesis times using a two-step simple hydrothermal method. The hydrothermal synthesis time of zinc sulfide affects the content and distribution of zinc sulfide spheres decorated on the surface of titanium dioxide petals. Liu et al. [56] successfully prepared uniform spherical zinc sulfide nanoparticles with a diameter of 5–10 nm using a simple hydrothermal method at a high temperature of 160 °C. In addition to the obvious blue shift, the prepared zinc sulfide nanoparticles also have higher PL intensity than normal micron-sized nanoparticles.

In this study, the generation of vacancies was primarily controlled by the addition of ethanolamine, while the concentration of vacancies was regulated by varying the reaction temperature. Using a solvothermal approach with zinc nitrate hexahydrate and thiourea at various temperatures, we prepared pink ZnS, which was analyzed through multiple characterization methods. The experimental results demonstrate that the optimal sample exhibits outstanding photocatalytic hydrogen evolution performance, achieving a hydrogen evolution rate of 7631.70  $\mu\text{mol h}^{-1} \text{g}^{-1}$ , significantly higher than that of other samples.

By introducing zinc vacancies, the bandgap of the material was effectively modulated, leading to a remarkable expansion of its visible light absorption range. Simultaneously, the introduction of zinc vacancies created abundant active sites on the material's surface, enhancing the separation efficiency of photogenerated electron-hole pairs and reducing the carrier recombination rate. These synergistic effects collectively improved the material's photocatalytic performance, resulting in significantly enhanced catalytic activity for visible-light-driven water splitting and hydrogen evolution.

## 2. Results and Discussion

The phase of the synthesized nanomaterials was determined by powder XRD. Figure 1 shows the crystal structures of ZnS-120, ZnS-140, ZnS-160, and ZnS-180. The diffraction peaks at  $27.12^\circ$ ,  $28.55^\circ$ ,  $30.62^\circ$ ,  $47.75^\circ$ , and  $56.69^\circ$  were observed in the XRD patterns, corresponding to the (100), (002), (101), (110), and (112) planes of ZnS, respectively. It is shown that the sample has a hexagonal wurtzite crystal structure. They have similar and strong diffraction peaks, indicating that they have good crystallinity. No other peaks were observed, indicating that it was pure ZnS. We can also observe the crystal plane and diffraction peak intensity of ZnS-120, ZnS-140, ZnS-160, and ZnS-180. With the increase in the preparation temperature of the samples, the peak of the sample becomes sharper and the crystallinity of the sample improves [57].

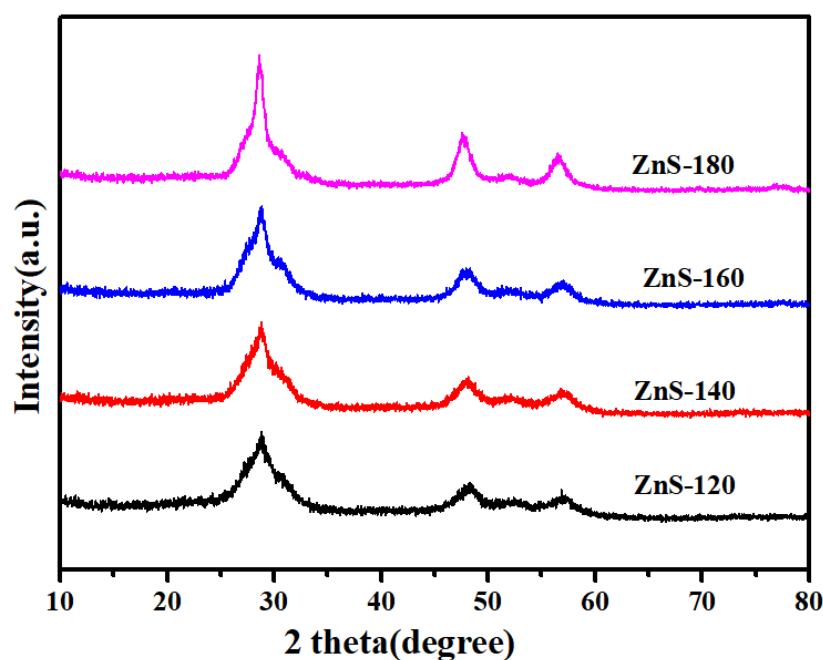


**Figure 1.** XRD patterns of ZnS-120, ZnS-140, ZnS-160, and ZnS-180.

To explore the differences between ZnS-120, ZnS-140, ZnS-160, and ZnS-180, we took pictures via SEM to observe the differences in their morphology. In general, the reaction temperature affects the growth and movement rate of the initial ZnS particles, as well as the particle diameter distribution. As the reaction temperature of the precursor solution increases, thiourea is decomposed,  $S^{2-}$  ions are formed slowly and uniformly, and  $Zn^{2+}$  ions react with  $S^{2-}$  ions to form ZnS nanocrystals [57]. The morphology maps generated by ZnS-120, ZnS-140, ZnS-160, and ZnS-180 are shown in Figure 2a–d, respectively. ZnS-120 and ZnS-140 are all flower spheres. The morphology of ZnS-160 and ZnS-180 samples showed a certain aggregation, but with the increase in the preparation temperature of the samples, the ZnS crystals grew to a smaller size. The smaller the particle size, the larger the specific surface area, which enhances the utilization of sunlight for photocatalytic water

splitting to produce hydrogen [58]. High-resolution TEM tests were conducted on ZnS-160 to observe and analyze its structure. From Figure 2e, we can see that for the 0.312 nm lattice spacing attributed to the wurtzite (002) plane, more lattice fringes were bent, broken, and blurred, indicating the formation of a vacancy.

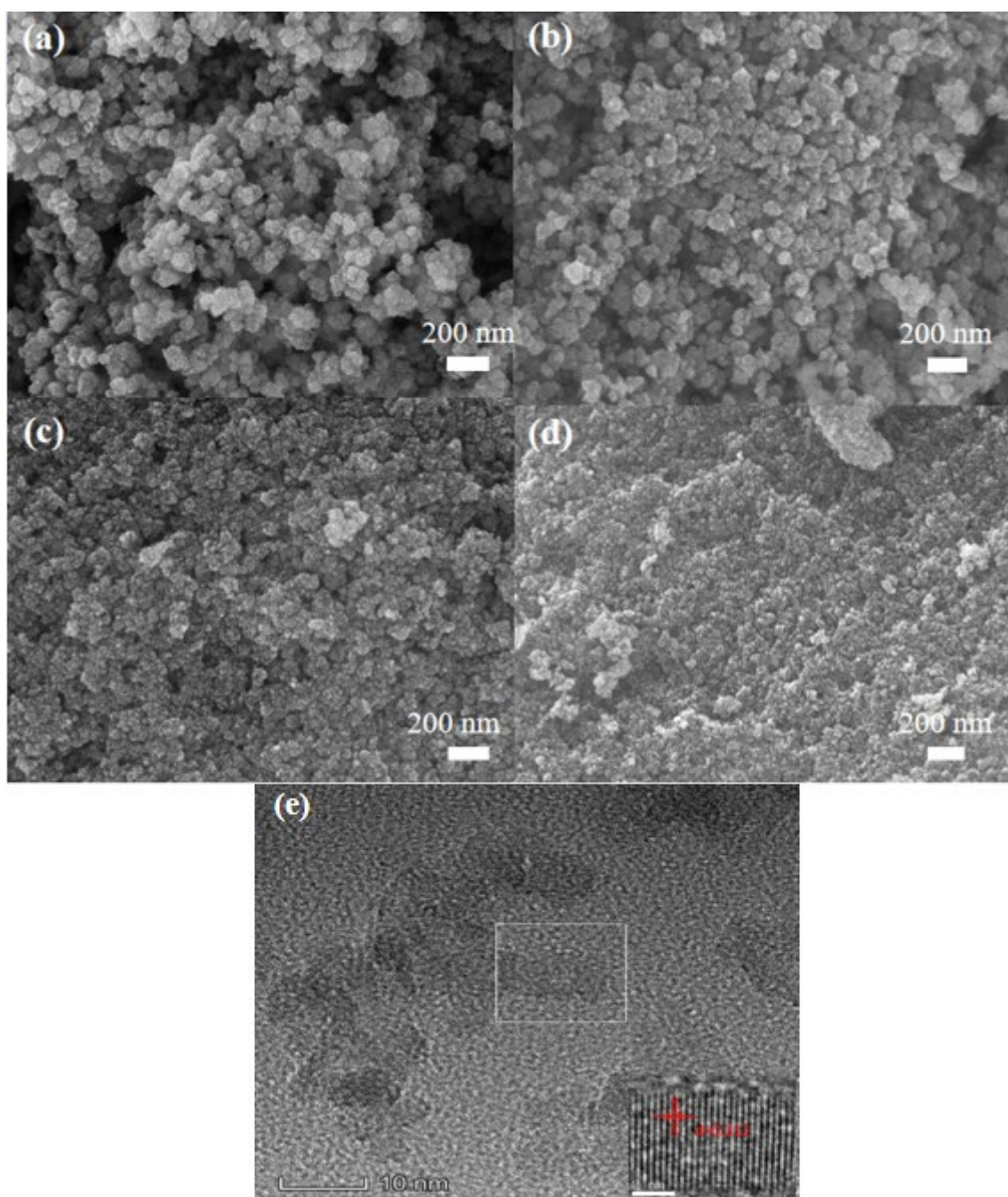


**Figure 2.** (a–d) SEM images of ZnS-120, ZnS-140, ZnS-160, and ZnS-180, respectively; (e) TEM image of ZnS-160.

Nitrogen adsorption–desorption isotherms of pink ZnS materials at different temperatures were tested. According to IUPAC classification, all four are type III isotherms with typical H3 hysteresis curve characteristics [15]. As shown in Figure 3, the specific surface areas of ZnS-120, ZnS-140, ZnS-160, and ZnS-180 are 151.9489 m<sup>2</sup>/g, 186.0362 m<sup>2</sup>/g, 205.4208 m<sup>2</sup>/g, and 214.1513 m<sup>2</sup>/g, respectively. The BET surface area of ZnS gradually increases with the increase in the preparation temperature of the samples. The ZnS-160



catalyst can provide more active sites and promote the charge carrier transport process, which is conducive to improving the photocatalytic performance.

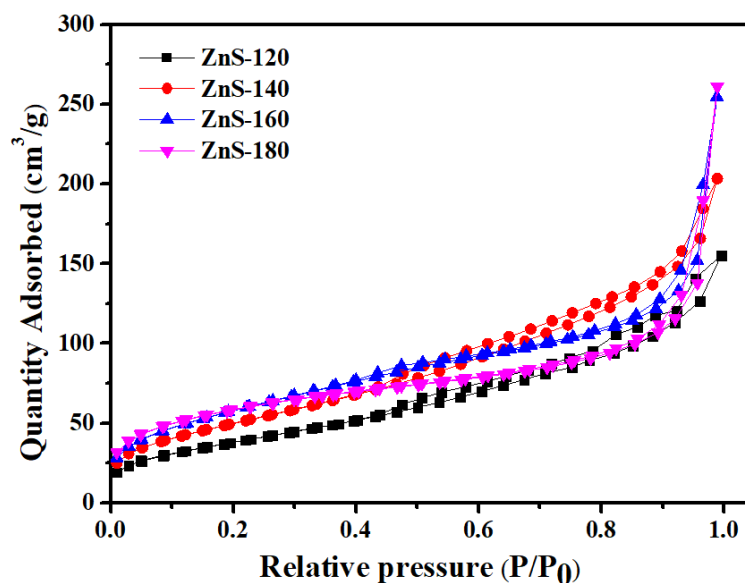


Figure 3. N<sub>2</sub> adsorption–desorption curve.

The optical properties of the synthesized photocatalyst were analyzed by UV-Vis diffuse reflectance spectroscopy. With BaSO<sub>4</sub> as the background, the wavelength measurement range is 300 nm–800 nm, and the photocatalyst (ZnS-120, ZnS-140, ZnS-160, and ZnS-180) is measured and analyzed by a solid ultraviolet-visible spectrophotometer. In Figure 4a, we observed strong absorption in the 300–340 nm UV region for ZnS-120, ZnS-140, ZnS-160, and ZnS-180. ZnS-120, ZnS-140, ZnS-160, and ZnS-180 have very steep edge absorption bands near 380 nm, which is the inherent absorption property of ZnS, and the absorption capacity of visible light is very small. However, the absorption of visible light by ZnS-160 samples at 500–550 nm is enhanced to a certain extent, which makes it possible for ZnS to utilize visible light sources. This phenomenon can be attributed to the introduction of vacancies in ZnS-160, which creates defect levels within the bandgap, thereby broadening the material's light absorption range and enabling it to absorb longer wavelengths of visible light [14]. The band gap of the semiconductor was calculated by the Tauc Plot method based on UV-Vis absorption spectra.

$$(Ah\nu)^2 = K(h\nu - E_g) \quad (1)$$

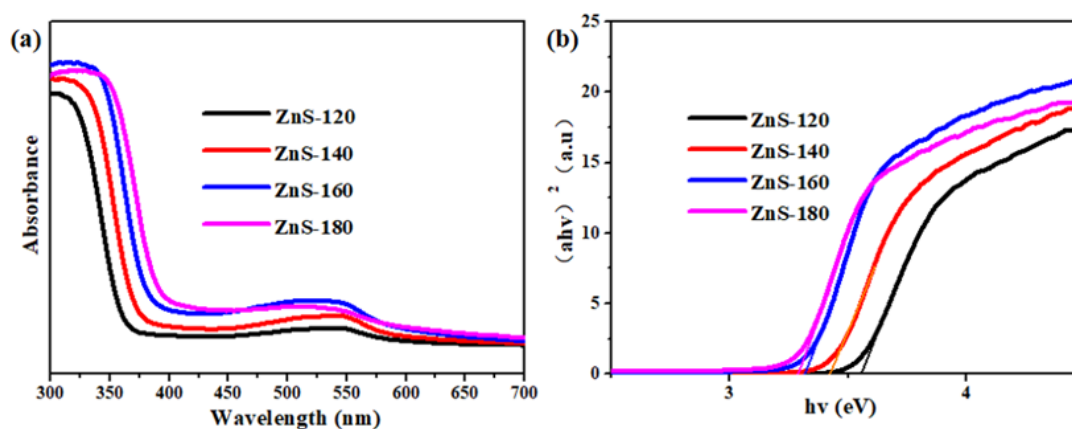


Figure 4. ZnS-120, ZnS-140, ZnS-160, and ZnS-180 (a) UV-Vis diffuse reflection diagram, (b) Tauc Plot.

Here,  $A$  is the absorbance,  $h\nu$  is the energy absorbed,  $K$  is the physical coefficient, and  $E_g$  is the energy band. In Figure 4b, it can be seen that nanometer ZnS has an obvious absorption peak at 340 nm. By extending the tangent line of the curve, the band gaps of ZnS-120, ZnS-140, ZnS-160, and ZnS-180 are 3.57, 3.48, 3.32, and 3.28 eV, respectively. The band gap between ZnS-160 and ZnS-180 is similar and relatively small, which is consistent with its high visible-light absorption intensity. With the increase in the preparation temperature of the samples, the bandgap of nano-ZnS is significantly reduced and the optical response range is expanded, which can improve the utilization of sunlight.

To further understand the electron transfer and electron–hole recombination behavior of the synthesized photocatalyst materials, we investigated their optical properties through photoluminescence (PL) spectroscopy. PL spectroscopy is used to obtain information related to the recombination and separation of photogenerated charge carriers in semiconductors [59]. The PL measurements were conducted at an excitation wavelength of 300 nm, with the emission spectrum recorded in the range of 350–550 nm. As shown in Figure 5, the PL spectra of ZnS-120, ZnS-140, ZnS-160, and ZnS-180 exhibit similar shapes. ZnS-120, ZnS-140, ZnS-160, and ZnS-180 display strong photoluminescence emission peaks at 390 nm. However, with the increase in the preparation temperature of the samples, the recombination of photogenerated carriers is significantly suppressed, leading to a substantial reduction in PL intensity. This indicates that the presence of vacancies can effectively reduce the recombination of electron–hole pairs. Notably, ZnS-160 exhibits significantly lower PL intensity compared to ZnS-120, ZnS-140, and ZnS-180, which is primarily attributed to the presence of vacancies. These vacancies effectively suppress electron–hole recombination, thereby substantially enhancing the photocatalytic hydrogen production performance.

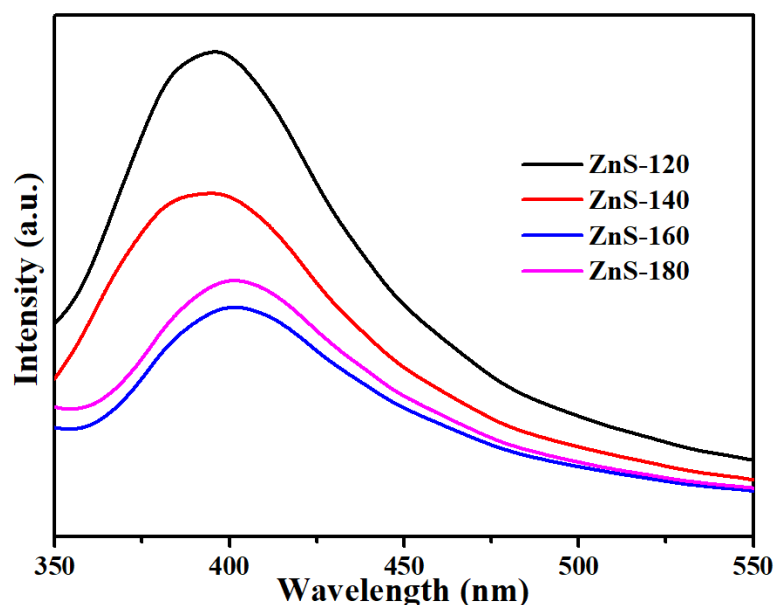


Figure 5. PL spectra of ZnS-120, ZnS-140, ZnS-160, and ZnS-180.

XPS was further employed to determine the binding energy states on the surfaces of samples prepared at different temperatures, thereby facilitating the analysis of the valence state composition of the elements within the samples. As shown in Figure 6, the sample is predominantly composed of Zn and S elements. The C 1s peak of surface amorphous carbon at 284.8 eV was utilized as a reference for calibration purposes. When the particle surfaces are exposed to air, the weak spectral signals of C and O are attributed to atmospheric contamination. Furthermore, no particularly prominent oxidized sulfur species, such as  $-\text{SO}_2$ , were detected. Therefore, the synthesized ZnS particles represent a high-purity compound free from impurities. In Figure 6a, the Zn 2p spectrum of ZnS-120 exhibits

two distinct peaks located at 1021.63 eV and 1044.60 eV, corresponding to the spin-orbit splitting components of Zn 2p<sub>3/2</sub> and Zn 2p<sub>1/2</sub>, respectively [60,61]. With the increase in the preparation temperature of the samples, the Zn 2p spectrum of ZnS-160 displays two characteristic peaks at binding energies of 1021.41 eV and 1044.43 eV. The Zn 2p orbital of the sample begins to shift toward lower binding energies, which is attributed to the formation of zinc vacancies [62]. As shown in Figure 6b, two peaks are observed for S 2p in ZnS-120 at 161.23 eV and 162.38 eV, which result from the spin-orbit splitting into S 2p<sub>3/2</sub> and S 2p<sub>1/2</sub>, respectively. The S 2p spectrum of ZnS-160 exhibits two peaks at 161.20 eV and 162.33 eV [63–65]. It can be observed that with the increase in the preparation temperature of the samples, the S 2p orbital exhibits a slight shift toward lower binding energies.

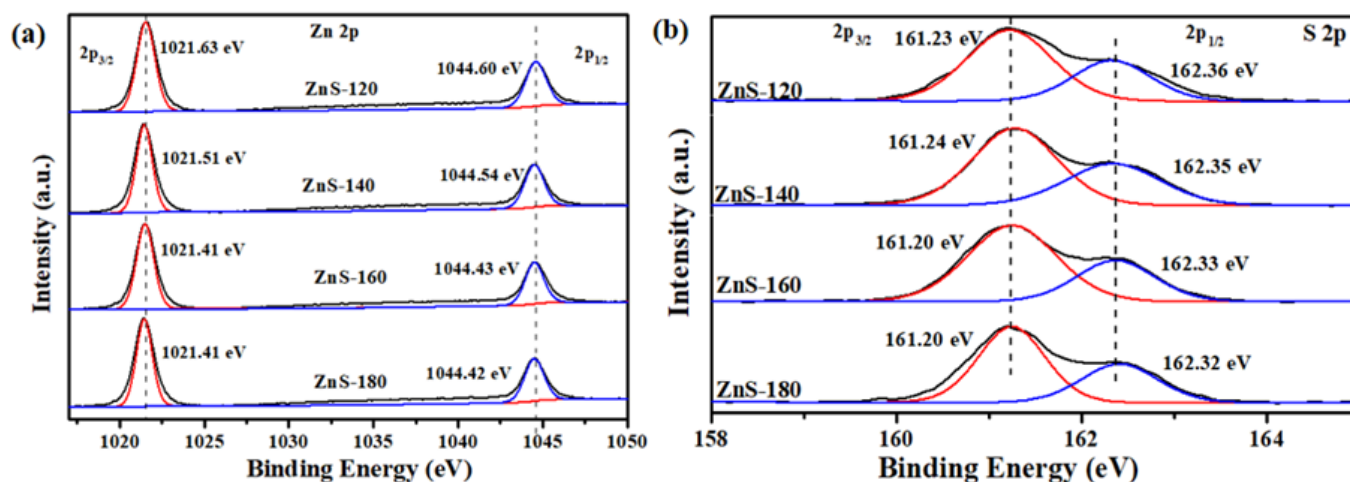
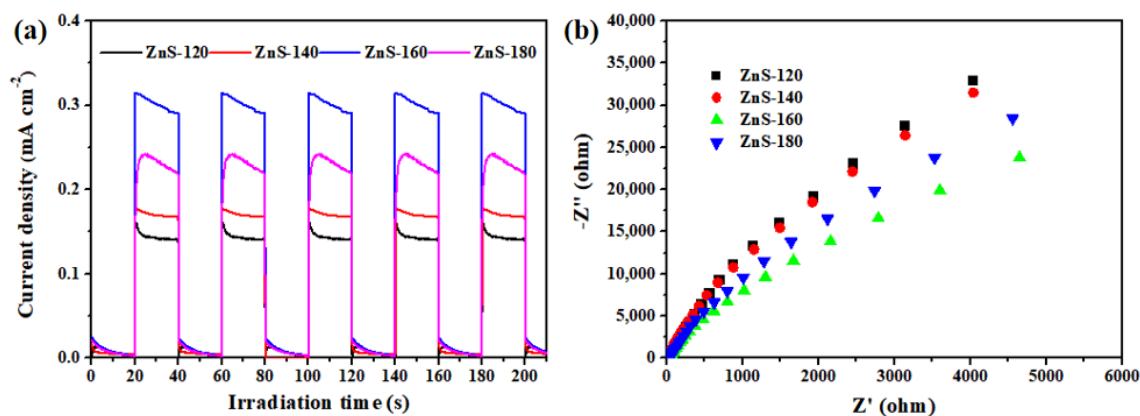


Figure 6. XPS spectra of (a) Zn 2p and (b) S 2p in ZnS-X samples.

In general, the electron–hole pairs generated in semiconductor photocatalysts must be effectively utilized for reduction and oxidation reactions during the photocatalytic process. However, the recombination of these electron–hole pairs will lead to poor catalytic performance. Therefore, to gain a deeper understanding of the photocatalytic mechanism, it is essential to investigate the separation and lifetime of charge carriers, specifically electron–hole pairs, on the photocatalyst surface. For this purpose, photoelectrochemical analysis was conducted to evaluate the excitation and transfer of carriers generated during the photocatalytic process. Figure 7a shows the transient photocurrent responses of ZnS-120, ZnS-140, ZnS-160, and ZnS-180, analyzed over several on–off cycles. When illuminated by a 300 W Xe lamp, all semiconductor catalysts exhibited a rapid photocurrent response. Notably, the photocurrent response of ZnS-160 was significantly higher than that of semiconductor catalysts ZnS-120, ZnS-140, and ZnS-180, indicating enhanced charge separation in the ZnS-160 sample. This suggests that a large number of carriers are rapidly excited under illumination, a phenomenon likely attributed to the presence of vacancies. Additionally, EIS was performed to study the charge transfer resistance and the separation efficiency of photogenerated electrons and holes during the photocatalytic reaction. The EIS Nyquist plots of ZnS-120, ZnS-140, ZnS-160, and ZnS-180 semiconductor nanomaterials are shown in Figure 7b. The radius in the EIS spectrum is proportional to the resistance of the electrode/electrolyte interface. As shown in Figure 7b, the radius of ZnS-160 is significantly smaller than that of ZnS-120, ZnS-140, and ZnS-180, indicating faster charge transfer and a lower recombination rate of photogenerated electron–hole pairs in ZnS-160. This property is highly beneficial for enhancing photocatalytic activity. This is consistent with the photocurrent results, indicating that vacancies facilitate the transport of charge carriers, further validating the superior photocatalytic performance of ZnS-160.



**Figure 7.** ZnS-120, ZnS-140, ZnS-160, and ZnS-180 (a) transient photocurrent response diagram and (b) electrochemical impedance diagram.

To investigate the practical application of the synthesized pink ZnS in UV-visible light-driven photocatalytic water splitting, the photocatalytic hydrogen evolution capability of ZnS-120, ZnS-140, ZnS-160, and ZnS-180 nanomaterials was evaluated under UV-visible light irradiation, using lactic acid aqueous solution as the sacrificial reagent, as shown in Figure 8a. The photocatalytic activity of ZnS-120, ZnS-140, ZnS-160, and ZnS-180 aligns with their overall photoelectric properties. Due to its limited visible-light response and the lowest charge transport and separation efficiency, ZnS-120 achieved a total hydrogen evolution of  $10,882.23 \mu\text{mol g}^{-1}$  over 6 h. With the increase in the preparation temperature of the samples, the hydrogen evolution performance of the samples improved, with ZnS-160 exhibiting the highest hydrogen evolution rate of  $45,790.18 \mu\text{mol g}^{-1}$ , approximately 4.21 times higher than that of ZnS-120. This indicates that the introduction of vacancies can significantly enhance the photocatalytic activity of the samples. To further understand the photocatalytic hydrogen evolution performance of these nanomaterials, their water-splitting capabilities were simulated under sunlight irradiation, again using lactic acid aqueous solution as the sacrificial reagent. In the absence of a co-catalyst, hydrogen evolution performance was tested solely under UV-visible light. The data given in Figure 8b correspond to the averaged hydrogen yield measured during 6 h of photocatalytic testing. The hydrogen evolution amounts for ZnS-120, ZnS-140, ZnS-160, and ZnS-180 were 1813.71, 4466.63, 7631.70, and 6134.46  $\mu\text{mol h}^{-1} \text{g}^{-1}$ , respectively. The relatively poor performance of ZnS-120 can be attributed to the rapid recombination of photoinduced carriers. ZnS-160 demonstrated the highest rate of  $7631.70 \mu\text{mol h}^{-1} \text{g}^{-1}$ , which is 4.21 times that of ZnS-120. This may be attributed to the presence of defects in ZnS-160, which facilitate faster charge transfer and a lower recombination rate of photogenerated electron-hole pairs, thereby significantly enhancing the photocatalytic activity. In addition, we conducted two control experiments, including a blank test without a catalyst and a test with zinc nitrate hexahydrate alone. The absence of hydrogen production in both cases unequivocally confirms that the hydrogen evolution activity originates from the pink ZnS catalyst. Additionally, Table S1 summarizes the hydrogen production performance of ZnS compared to different catalysts, demonstrating that the prepared pink ZnS-160 exhibits superior hydrogen production performance relative to other photocatalysts. The recyclability of ZnS-160 was further evaluated over four cycles. After each cycle, the catalyst was recovered by centrifugation and drying, with minimal loss observed. As shown in Figure 8c, the photocatalytic hydrogen evolution volume of ZnS-160 reached  $45,790.18 \mu\text{mol g}^{-1}$  during the first cycle. While the hydrogen evolution volume remained relatively stable over the first three cycles, a slight decrease was observed in the fourth cycle, likely due to minor photocorrosion under prolonged irradiation. Despite this, ZnS-160 maintained its superior



photocatalytic activity compared to other samples, demonstrating its potential as a robust photocatalyst for continuous hydrogen evolution under UV-visible light.

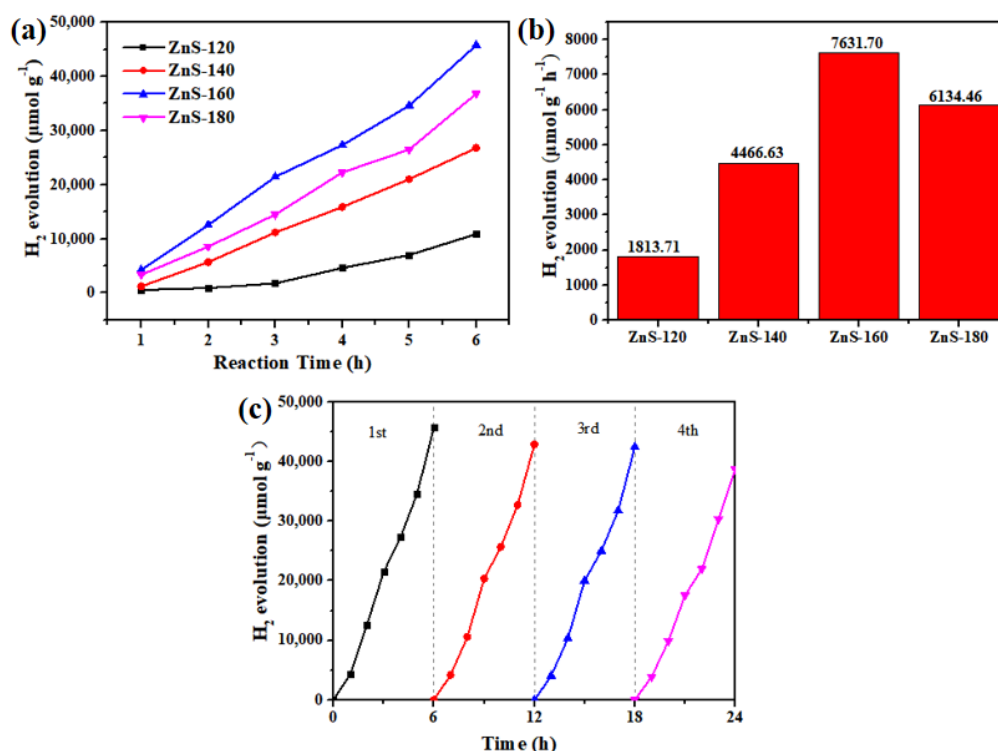


**Figure 8.** ZnS-120, ZnS-140, ZnS-160, and ZnS-180 (a) hydrogen production capacity, (b) hydrogen production rate, and (c) hydrogen production cycle diagram of ZnS-160.

Based on the aforementioned results, we propose a plausible mechanism for the photocatalytic hydrogen evolution of pink ZnS-160 semiconductor materials, as illustrated in Figure 9. The valence band and conduction band energy positions of a semiconductor can be calculated according to the following formula:  $E(\text{VB}) = X - E_e - 0.5E_g$  and  $E(\text{VB}) = E(\text{CB}) + E_g$ , where  $X$  represents the Mulliken's electronegativity of the semiconductor and the value of  $X$  is 5.26 eV for ordinary ZnS.  $E_e$  and  $E_g$  are the energy of the free electron on the hydrogen scale (about 4.5 eV vs. NHE) and the band gap energy of the semiconductor, respectively. The bandgap of ordinary ZnS is 3.6 eV, and through this calculation, the valence band and conduction band potentials of ordinary ZnS are +2.26 eV and −1.04 eV, respectively. Under simulated natural light irradiation, pink ZnS-160 is excited to generate photogenerated electrons and holes. XPS analysis reveals the presence of defects in the pink ZnS-160. According to solid UV-Vis diffuse reflectance spectroscopy and the Tauc equation, ZnS-160 exhibits a significant visible-light response and a reduced bandgap. Based on Figure S1, the valence band position of pink ZnS-160 is determined to be 0.85 eV, indicating that the introduction of vacancies elevates the valence band position compared to ordinary ZnS. This shift significantly weakens the oxidation capability of the holes, thereby protecting ZnS from photocorrosion. Additionally, the zinc vacancies introduce defect levels within the bandgap, which lower the energy required for carrier excitation and enhance the separation efficiency of photogenerated electrons and holes. Under UV-visible light irradiation, electrons in the valence band are excited to the conduction band of ZnS. The conduction band potential of ZnS is more negative than the  $H^+/H_2$  redox potential, satisfying the thermodynamic requirements for hydrogen evolution. The free  $H^+$  ions in the sacrificial agent solution combine with electrons in the conduction band to form  $H_2$ , while the holes in the valence band oxidize lactic acid to generate oxidation products.

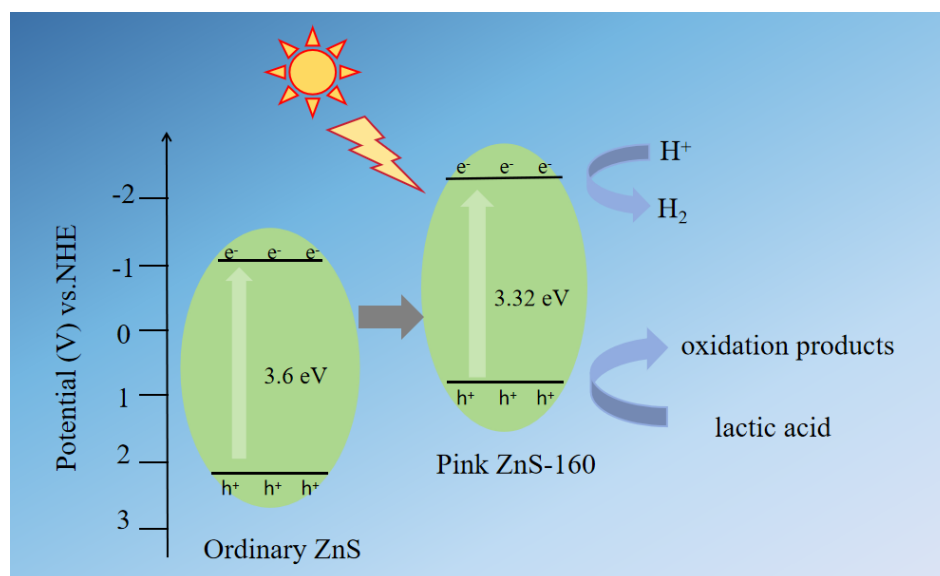


**Figure 9.** ZnS-160 photocatalytic hydrogen production mechanism.

### 3. Experimental Section

#### 3.1. Materials

All reagents are analytical grade reagents, and the purchased chemicals are AR grade (purity 99%). Zinc nitrate hexahydrate (Sinopharm Chemical Reagent Co., Ltd., Shanghai, China), thiourea (Xilong Scientific Co., Ltd., Shantou, China), ethanolamine (Sinopharm Chemical Reagent Co., Ltd., Shanghai, China), polyvinylpyrrolidone (Shanghai Macklin Biochemical Co., Ltd., Shanghai, China). Deionized water was used in all the synthesis processes.

#### 3.2. Preparation of Pink ZnS

Pink ZnS samples were prepared using the hydrothermal method. First, 2.38 g of zinc nitrate hexahydrate and 0.609 g of thiourea were dissolved in 30 mL of deionized water and 10 mL of ethanolamine and stirred for 40 min. Then, we added 0.05 g of polyvinylpyrrolidone, stirred the solution for 40 min, and transferred it to polytetrafluoroethylene lining. The solid powder obtained by heating at 120 °C for 4 h was centrifuged, washed four times with deionized water, and dried in an oven at 75 °C for 10 h. It is named ZnS-120. According to the above operation, they were heated to 140 °C, 160 °C, and 180 °C, respectively, and labeled as ZnS-140, ZnS-160, and ZnS-180 according to the heating temperature.

#### 3.3. Characterization

X-ray diffraction (XRD) data were tested using a Bruker D8 Advanced X-ray powder diffractometer (Rigaku Corp, Tokyo, Japan) with Cu-K $\alpha$  radiation ( $\lambda = 1.5418 \text{ \AA}$ ). The morphologies of the as-prepared samples were analyzed using scanning electron microscopy (SEM, S-4800, Hitachi, Tokyo, Japan). The crystal structures were observed using a JEM-2100 F transmission electron microscope (TEM, JEOL, Tokyo, Japan). The UV-Vis diffuse reflectance spectra (DRS) were acquired using a UV-2550 spectrophotometer (Shimadzu, Tokyo, Japan). Photoluminescence (PL) spectra were measured at room temperature using a spectrophotometer (F97Pro, Leng guang, Shanghai, China). The photocurrent density, EIS, and Mott–Schottky were measured by a CHI 760E electrochemical workstation (Shanghai, China). Further insight into the elemental composition was determined by XPS (X-ray photoelectron spectroscopy) spectra captured on the ESCALAB 250 Xi-XPS system with Al K $\alpha$  radiation.

### 3.4. Photocurrent Measurements

A three-electrode system, comprising counter, reference, and working electrodes of Pt-wire, Ag/AgCl (in saturated KCl), and the prepared material, respectively, was employed to evaluate the photocurrent measurements. First, 5 mg of the catalyst was dissolved in a mixed solution of 1 mL of anhydrous ethanol and 50  $\mu$ L of Nafion solution and treated under ultrasound for 2 h to fully disperse the catalyst. Then, 200  $\mu$ L of the mixed solution was dropped on a  $2 \times 2$  cm clean conductive glass sheet as a working electrode. A 300 W Xe lamp was used as the light source.

### 3.5. Photocatalytic Hydrogen Production Activity

In order to evaluate the hydrogen production efficiency, 50 mg of the sample was first weighed, added to a sacrificial agent (10 mL of lactic acid), dispersed in a 100 mL round-bottom flask containing 40 mL of deionized water, and stirred evenly. Exhaust air was removed by blowing argon for 20 min. The sample was sealed and then placed in a circular groove for fixation. The magnetic stirrer was turned on, the condensate device was turned on, and the sample was irradiated with a Xe lamp under ultraviolet-visible light. Sampling was performed every 1 h, and hydrogen production was detected using a gas chromatograph with a carrier gas of Ar.

## 4. Conclusions

In summary, this study employed a conventional solvothermal method to synthesize pink defect ZnS using zinc nitrate hexahydrate and thiourea. Under the synthesis condition of 160 °C, ZnS-160 exhibited an absorption peak within the range of 500–550 nm, which enhanced its visible light absorption and improved the separation efficiency of electrons and holes. Through the introduction of vacancies, the band gap of the material was effectively modulated, significantly extending its visible-light absorption range. Simultaneously, the incorporation of zinc vacancies created abundant active sites on the material surface, enhancing the separation efficiency of photogenerated electron–hole pairs and reducing the carrier recombination rate, and improving the photocatalytic hydrogen evolution efficiency. More importantly, the introduction of vacancies upshifts the valence band position, thereby reducing the oxidation capability of the holes and effectively suppressing the photocorrosion of ZnS. Furthermore, this study is expected to provide valuable insights for enhancing the hydrogen evolution performance of individual materials. This work offers a novel strategy for the further design of ZnS-based photocatalysts.

**Supplementary Materials:** The following supporting information can be downloaded at: <https://www.mdpi.com/article/10.3390/inorganics13050166/s1>, Figure S1: The VB XPS spectrum of ZnS-160; Table S1: Comparison of photocatalytic hydrogen production performance among different ZnS catalysts. References [66–70] are cited in the supplementary materials.

**Author Contributions:** Conceptualization, H.L.; Methodology, S.G., H.L. and J.Z.; Validation, S.G., Y.L., T.M., H.L. and J.Z.; Formal analysis, S.G., T.M. and J.Z.; Investigation, S.G., Y.L. and T.M.; Data curation, S.G. and Y.L.; Writing—original draft, S.G. and Y.L.; Writing—review & editing, T.M. and H.L.; Supervision, H.L.; Project administration, H.L.; Funding acquisition, H.L. All authors have read and agreed to the published version of the manuscript.

**Funding:** This work was financially supported by the National Natural Science Foundation of China (No. 22275103), the Science and Technology Small and Medium-sized Enterprise Innovation Ability Enhancement Project of Shandong Province (No. 2023TSGC0676, 2022TSGC2467), and the Industry–University–Research Collaborative Innovation Foundation (2022CXY-01, 2021KC03).

**Data Availability Statement:** The original contributions presented in the study are included in the article/Supplementary Material, further inquiries can be directed to the corresponding authors.

**Conflicts of Interest:** The authors declare no conflict of interest.

## References

1. Raza, W.; Kerketta, U.; Hwang, I.; Schmuki, P. CdS Decorated on Hierarchically Structured Single Crystal TiO<sub>2</sub> Nanosheets for Enhanced Photoelectrochemical H<sub>2</sub> Generation. *ChemElectroChem* **2022**, *9*, e202200706. [\[CrossRef\]](#)
2. Raza, W.; Ahmad, K.; Alvarado, F.G.; Oh, T.H. Progress in 2D MoS<sub>2</sub>-Based Advanced Materials for Hydrogen Evolution and Energy Storage Applications. *Inorganics* **2025**, *13*, 47. [\[CrossRef\]](#)
3. Raza, W.; Ahmad, K.; Khan, R.A.; Kim, H. Ag decorated ZnO for enhanced photocatalytic H<sub>2</sub> generation and pollutant degradation. *Int. J. Hydrogen Energy* **2023**, *48*, 29071–29081. [\[CrossRef\]](#)
4. Osuagwu, B.; Raza, W.; Tesler, A.B.; Schmuki, P. A drastic improvement in photocatalytic H<sub>2</sub> production by TiO<sub>2</sub> nanosheets grown directly on Ta<sub>2</sub>O<sub>5</sub> substrates. *Nanoscale* **2021**, *13*, 12750–12756. [\[CrossRef\]](#)
5. She, H.; Ma, X.; Chen, K.; Liu, H.; Huang, J.; Wang, L.; Wang, Q. Photocatalytic H<sub>2</sub> production activity of TiO<sub>2</sub> modified by inexpensive Cu(OH)<sub>2</sub> cocatalyst. *J. Alloys Compd.* **2020**, *821*, 153239. [\[CrossRef\]](#)
6. Qin, Z.; Chen, L.; Ma, R.; Tomovska, R.; Luo, X.; Xie, X.; Su, T.; Ji, H. TiO<sub>2</sub>/BiYO<sub>3</sub> composites for enhanced photocatalytic hydrogen production. *J. Alloys Compd.* **2020**, *836*, 155428. [\[CrossRef\]](#)
7. Park, Y.-K.; Kim, B.-J.; Jeong, S.; Jeon, K.-J.; Chung, K.-H.; Jung, S.-C. Characteristics of hydrogen production by photocatalytic water splitting using liquid phase plasma over Ag-doped TiO<sub>2</sub> photocatalysts. *Environ. Res.* **2020**, *188*, 109630. [\[CrossRef\]](#)
8. Han, X.; An, L.; Hu, Y.; Li, Y.; Hou, C.; Wang, H.; Zhang, Q. Ti<sub>3</sub>C<sub>2</sub> MXene-derived carbon-doped TiO<sub>2</sub> coupled with g-C<sub>3</sub>N<sub>4</sub> as the visible-light photocatalysts for photocatalytic H<sub>2</sub> generation. *Appl. Catal. B Environ.* **2020**, *265*, 118539. [\[CrossRef\]](#)
9. Raza, W.; Haque, M.M.; Muneer, M.; Fleisch, M.; Hakki, A.; Bahnemann, D. Photocatalytic degradation of different chromophoric dyes in aqueous phase using La and Mo doped TiO<sub>2</sub> hybrid carbon spheres. *J. Alloys Compd.* **2015**, *632*, 837–844. [\[CrossRef\]](#)
10. Raza, W.; Haque, M.M.; Muneer, M.; Bahnemann, D. Synthesis of visible light driven TiO<sub>2</sub> coated carbon nanospheres for degradation of dyes. *Arab. J. Chem.* **2019**, *12*, 3534–3545. [\[CrossRef\]](#)
11. Raza, W.; Hwang, I.; Denisov, N.; Schmuki, P. Thermal Ramping Rate during Annealing of TiO<sub>2</sub> Nanotubes Greatly Affects Performance of Photoanodes. *Phys. Status Solidi A* **2021**, *218*, 2100040. [\[CrossRef\]](#)
12. Wang, J.; Zhao, Y.; Li, G.; Luo, D.; Liu, J.; Zhang, Y.; Wang, X.; Shui, L.; Chen, Z. Aligned sulfur-deficient ZnS<sub>1-x</sub> nanotube arrays as efficient catalyzer for high-performance lithium/sulfur batteries. *Nano Energy* **2021**, *84*, 105891. [\[CrossRef\]](#)
13. Xiao, B.; Lv, T.; Zhao, J.; Rong, Q.; Zhang, H.; Wei, H.; He, J.; Zhang, J.; Zhang, Y.; Peng, Y.; et al. Synergistic Effect of the Surface Vacancy Defects for Promoting Photocatalytic Stability and Activity of ZnS Nanoparticles. *ACS Catal.* **2021**, *11*, 13255–13265. [\[CrossRef\]](#)
14. Zhou, J.; Zhao, J.; Liu, R. Defect engineering of zeolite imidazole framework derived ZnS nanosheets towards enhanced visible light driven photocatalytic hydrogen production. *Appl. Catal. B Environ.* **2020**, *278*, 119265. [\[CrossRef\]](#)
15. Gao, F.; Lei, R.; Huang, X.; Yuan, J.; Jiang, C.; Feng, W.; Zhang, L.; Liu, P. In situ etching growth of defective ZnS nanosheets anchored vertically on layered-double-hydroxide microflowers for accelerated photocatalytic activity. *Appl. Catal. B Environ.* **2021**, *292*, 120187. [\[CrossRef\]](#)
16. Goto, Y.; Hisatomi, T.; Wang, Q.; Higashi, T.; Ishikiriya, K.; Maeda, T.; Sakata, Y.; Okunaka, S.; Tokudome, H.; Katayama, M.; et al. A Particulate Photocatalyst Water-Splitting Panel for Large-Scale Solar Hydrogen Generation. *Joule* **2018**, *2*, 509–520. [\[CrossRef\]](#)
17. Wang, Q.; Hisatomi, T.; Jia, Q.; Tokudome, H.; Zhong, M.; Wang, C.; Pan, Z.; Takata, T.; Nakabayashi, M.; Shibata, N.; et al. Scalable water splitting on particulate photocatalyst sheets with a solar-to-hydrogen energy conversion efficiency exceeding 1%. *Nat. Mater.* **2016**, *15*, 611–615. [\[CrossRef\]](#)
18. Wang, Z.; Li, C.; Domen, K. Recent developments in heterogeneous photocatalysts for solar-driven overall water splitting. *Chem. Soc. Rev.* **2019**, *48*, 2109–2125. [\[CrossRef\]](#)
19. Waqas, M.; Wei, Y.; Mao, D.; Qi, J.; Yang, Y.; Wang, B.; Wang, D. Multi-shelled TiO<sub>2</sub>/Fe<sub>2</sub>TiO<sub>5</sub> heterostructured hollow microspheres for enhanced solar water oxidation. *Nano Res.* **2017**, *10*, 3920–3928. [\[CrossRef\]](#)
20. Wei, Y.; Wang, J.; Yu, R.; Wan, J.; Wang, D. Constructing SrTiO<sub>3</sub>-TiO<sub>2</sub> Heterogeneous Hollow Multi-shelled Structures for Enhanced Solar Water Splitting. *Angew. Chem. Int. Ed.* **2019**, *58*, 1422–1426. [\[CrossRef\]](#)
21. Wang, L.; Wan, J.; Zhao, Y.; Yang, N.; Wang, D. Hollow Multi-Shelled Structures of Co<sub>3</sub>O<sub>4</sub> Dodecahedron with Unique Crystal Orientation for Enhanced Photocatalytic CO<sub>2</sub> Reduction. *J. Am. Chem. Soc.* **2019**, *141*, 2238–2241. [\[CrossRef\]](#) [\[PubMed\]](#)
22. You, F.; Wan, J.; Qi, J.; Mao, D.; Yang, N.; Zhang, Q.; Gu, L.; Wang, D. Lattice Distortion in Hollow Multi-Shelled Structures for Efficient Visible-Light CO<sub>2</sub> Reduction with a SnS<sub>2</sub>/SnO<sub>2</sub> Junction. *Angew. Chem. Int. Ed.* **2019**, *59*, 721–724. [\[CrossRef\]](#) [\[PubMed\]](#)
23. Meng, X.; Zuo, G.; Zong, P.; Pang, H.; Ren, J.; Zeng, X.; Liu, S.; Shen, Y.; Zhou, W.; Ye, J. A rapidly room-temperature-synthesized Cd/ZnS:Cu nanocrystal photocatalyst for highly efficient solar-light-powered CO<sub>2</sub> reduction. *Appl. Catal. B Environ.* **2018**, *237*, 68–73. [\[CrossRef\]](#)

24. Chen, J.; Xin, F.; Qin, S.; Yin, X. Photocatalytically reducing CO<sub>2</sub> to methyl formate in methanol over ZnS and Ni-doped ZnS photocatalysts. *Chem. Eng. J.* **2013**, *230*, 506–512. [\[CrossRef\]](#)
25. Amaranatha Reddy, D.; Ma, R.; Choi, M.Y.; Kim, T.K. Reduced graphene oxide wrapped ZnS–Ag<sub>2</sub>S ternary composites synthesized via hydrothermal method: Applications in photocatalyst degradation of organic pollutants. *Appl. Surf. Sci.* **2015**, *324*, 725–735. [\[CrossRef\]](#)
26. Wang, Q.; Wang, P.; Xu, P.; Li, Y.; Duan, J.; Zhang, G.; Hu, L.; Wang, X.; Zhang, W. Visible-light-driven photo-Fenton reactions using Zn<sub>1–1.5</sub>Fe<sub>x</sub>S/g-C<sub>3</sub>N<sub>4</sub> photocatalyst: Degradation kinetics and mechanisms analysis. *Appl. Catal. B Environ.* **2020**, *266*, 118653. [\[CrossRef\]](#)
27. Yu, S.; Fan, X.-B.; Wang, X.; Li, J.; Zhang, Q.; Xia, A.; Wei, S.; Wu, L.-Z.; Zhou, Y.; Patzke, G.R. Efficient photocatalytic hydrogen evolution with ligand engineered all-inorganic InP and InP/ZnS colloidal quantum dots. *Nat. Commun.* **2018**, *9*, 4009. [\[CrossRef\]](#)
28. Xie, Y.P.; Yu, Z.B.; Liu, G.; Ma, X.L.; Cheng, H.-M. CdS–mesoporous ZnS core–shell particles for efficient and stable photocatalytic hydrogen evolution under visible light. *Energy Environ. Sci.* **2014**, *7*, 1895–1901. [\[CrossRef\]](#)
29. Li, P.; Luo, G.; Zhu, S.; Guo, L.; Qu, P.; He, T. Unraveling the selectivity puzzle of H<sub>2</sub> evolution over CO<sub>2</sub> photoreduction using ZnS nanocatalysts with phase junction. *Appl. Catal. B Environ.* **2020**, *274*, 119115. [\[CrossRef\]](#)
30. Hong, Y.P.; Zhang, J.; Huang, F.; Zhang, J.Y.; Wang, X.; Wu, Z.C.; Lin, Z.; Yu, J.G. Enhanced visible light photocatalytic hydrogen production activity of CuS/ZnS nanoflower spheres. *J. Mater. Chem. A* **2015**, *3*, 13913–13919. [\[CrossRef\]](#)
31. Zhou, C.; Ma, Z.; Ren, Z.; Mao, X.; Dai, D.; Yang, X. Effect of defects on photocatalytic dissociation of methanol on TiO<sub>2</sub>(110). *Chem. Sci.* **2011**, *2*, 1980–1983. [\[CrossRef\]](#)
32. Kong, M.; Li, Y.; Chen, X.; Tian, T.; Fang, P.; Zheng, F.; Zhao, X. Tuning the Relative Concentration Ratio of Bulk Defects to Surface Defects in TiO<sub>2</sub> Nanocrystals Leads to High Photocatalytic Efficiency. *J. Am. Chem. Soc.* **2011**, *133*, 16414–16417. [\[CrossRef\]](#) [\[PubMed\]](#)
33. Long, R.; English, N.J.; Prezhdo, O.V. Defects Are Needed for Fast Photo-Induced Electron Transfer from a Nanocrystal to a Molecule: Time-Domain Ab Initio Analysis. *J. Am. Chem. Soc.* **2013**, *135*, 18892–18900. [\[CrossRef\]](#) [\[PubMed\]](#)
34. Zhang, J.; Xu, Q.; Feng, Z.; Li, M.; Li, C. Importance of the Relationship between Surface Phases and Photocatalytic Activity of TiO<sub>2</sub>. *Angew. Chem.* **2008**, *120*, 1790–1793. [\[CrossRef\]](#)
35. Wang, X.; Xu, Q.; Li, M.; Shen, S.; Wang, X.; Wang, Y.; Feng, Z.; Shi, J.; Han, H.; Li, C. Photocatalytic Overall Water Splitting Promoted by an α–β phase Junction on Ga<sub>2</sub>O<sub>3</sub>. *Angew. Chem. Int. Ed.* **2012**, *51*, 13089–13092. [\[CrossRef\]](#)
36. Zhou, C.; Ren, Z.; Tan, S.; Ma, Z.; Mao, X.; Dai, D.; Fan, H.; Yang, X.; LaRue, J.; Cooper, R.; et al. Site-specific photocatalytic splitting of methanol on TiO<sub>2</sub>(110). *Chem. Sci.* **2010**, *1*, 575–580. [\[CrossRef\]](#)
37. Yu, J.; Low, J.; Xiao, W.; Zhou, P.; Jaroniec, M. Enhanced Photocatalytic CO<sub>2</sub>-Reduction Activity of Anatase TiO<sub>2</sub> by Coexposed {001} and {101} Facets. *J. Am. Chem. Soc.* **2014**, *136*, 8839–8842. [\[CrossRef\]](#)
38. Liu, S.; Wang, X.; Wang, K.; Lv, R.; Xu, Y. ZnO/ZnS–PdS core/shell nanorods: Synthesis, characterization and application for photocatalytic hydrogen production from a glycerol/water solution. *Appl. Surf. Sci.* **2013**, *283*, 732–739. [\[CrossRef\]](#)
39. Hao, X.; Wang, Y.; Zhou, J.; Cui, Z.; Wang, Y.; Zou, Z. Zinc vacancy-promoted photocatalytic activity and photostability of ZnS for efficient visible-light-driven hydrogen evolution. *Appl. Catal. B Environ.* **2018**, *221*, 302–311. [\[CrossRef\]](#)
40. Altiokka, B. Effects of Inhibitor on ZnS Thin Films Fabricated by Electrodeposition. *J. Electron. Mater.* **2019**, *48*, 2398–2403. [\[CrossRef\]](#)
41. Charinpanitkul, T.; Chanagul, A.; Dutta, J.; Rungsardthong, U.; Tanthapanichakoon, W. Effects of cosurfactant on ZnS nanoparticle synthesis in microemulsion. *Sci. Technol. Adv. Mater.* **2005**, *6*, 266–271. [\[CrossRef\]](#)
42. Yu, L.; Ruan, H.; Zheng, Y.; Li, D. A facile solvothermal method to produce ZnS quantum dots-decorated graphene nanosheets with superior photoactivity. *Nanotechnology* **2013**, *24*, 375601. [\[CrossRef\]](#) [\[PubMed\]](#)
43. Goktas, A.; Tumbul, A.; Aslan, F. A new approach to growth of chemically depositable different ZnS nanostructures. *J. Sol-Gel Sci. Technol.* **2019**, *90*, 487–497. [\[CrossRef\]](#)
44. Shanmugam, N.; Cholan, S.; Kannadasan, N.; Sathishkumar, K.; Viruthagiri, G. Effect of polyvinylpyrrolidone as capping agent on Ce<sup>3+</sup> doped flowerlike ZnS nanostructure. *Solid State Sci.* **2014**, *28*, 55–60. [\[CrossRef\]](#)
45. Varma, A.; Mukasyan, A.S.; Rogachev, A.S.; Manukyan, K.V. Solution Combustion Synthesis of Nanoscale Materials. *Chem. Rev.* **2016**, *116*, 14493–14586. [\[CrossRef\]](#)
46. Hrubaru, M.; Onwudiwe, D.C.; Hosten, E. Synthesis and properties of ZnS nanoparticles by solvothermal and pyrolysis routes using the Zn dithiocarbamate complex as novel single source precursor. *J. Sulfur Chem.* **2015**, *37*, 37–47. [\[CrossRef\]](#)
47. Sabaghi, V.; Davar, F.; Fereshteh, Z. ZnS nanoparticles prepared via simple reflux and hydrothermal method: Optical and photocatalytic properties. *Ceram. Int.* **2018**, *44*, 7545–7556. [\[CrossRef\]](#)
48. Jadraque, M.; Evtushenko, A.B.; Ávila-Brande, D.; López-Arias, M.; Lorient, V.; Shukhov, Y.G.; Kibis, L.S.; Bulgakov, A.V.; Martín, M. Co-Doped ZnS Clusters and Nanostructures Produced by Pulsed Laser Ablation. *J. Phys. Chem. C* **2013**, *117*, 5416–5423. [\[CrossRef\]](#)



49. Palve, A.M. Deposition of Zinc Sulfide Thin Films from Zinc(II) Thiosemicarbazones as Single Molecular Precursors Using Aerosol Assisted Chemical Vapor Deposition Technique. *Front. Mater.* **2019**, *6*, 46. [\[CrossRef\]](#)
50. Zhang, Y.C.; Wang, G.Y.; Hu, X.Y.; Shi, Q.F.; Qiao, T.; Yang, Y. Phase-controlled synthesis of ZnS nanocrystallites by mild solvothermal decomposition of an air-stable single-source molecular precursor. *J. Cryst. Growth* **2005**, *284*, 554–560. [\[CrossRef\]](#)
51. Zhang, Y.C.; Du, Z.N.; Li, K.W.; Zhang, M. Size-controlled hydrothermal synthesis of SnS<sub>2</sub> nanoparticles with high performance in visible light-driven photocatalytic degradation of aqueous methyl orange. *Sep. Purif. Technol.* **2011**, *81*, 101–107. [\[CrossRef\]](#)
52. Zhang, Y.C.; Tang, J.Y.; Hu, X.Y. Controllable synthesis and magnetic properties of pure hematite and maghemite nanocrystals from a molecular precursor. *J. Alloys Compd.* **2008**, *462*, 24–28. [\[CrossRef\]](#)
53. Bai, J.; Sun, J.; Zhu, X.; Liu, J.; Zhang, H.; Yin, X.B.; Liu, L. Enhancement of Solar-Driven Photocatalytic Activity of BiOI Nanosheets through Predominant Exposed High Energy Facets and Vacancy Engineering. *Small* **2020**, *16*, e1904783. [\[CrossRef\]](#) [\[PubMed\]](#)
54. Xu, S.H.; Fei, G.T.; Huang, J.Y.; Xia, K.; Wang, B. Controllable hydrothermal synthesis of hollow ZnS nanospheres: Morphological evolution mechanism and photocatalytic performance. *Ceram. Int.* **2024**, *50*, 1556–1563. [\[CrossRef\]](#)
55. Liang, Y.-C.; Wang, C.-C. Hydrothermally derived zinc sulfide sphere-decorated titanium dioxide flower-like composites and their enhanced ethanol gas-sensing performance. *J. Alloys Compd.* **2018**, *730*, 333–341. [\[CrossRef\]](#)
56. Liu, J.; Ma, J.; Liu, Y.; Song, Z.; Sun, Y.; Fang, J.; Liu, Z. Synthesis of ZnS nanoparticles via hydrothermal process assisted by microemulsion technique. *J. Alloys Compd.* **2009**, *486*, L40–L43. [\[CrossRef\]](#)
57. Park, S.-J.; Song, J.-H. Glycothermally Synthesized Self-aggregated ZnS Spherical Particles for Methyl Orange Photodecomposition. *Korean J. Met. Mater.* **2021**, *59*, 732–740. [\[CrossRef\]](#)
58. Zaki, M.I.; Fouad, N.E.; Mekhemer, G.A.H.; Jagadale, T.C.; Ogale, S.B. TiO<sub>2</sub> nanoparticle size dependence of porosity, adsorption and catalytic activity. *Colloids Surf. A Physicochem. Eng. Asp.* **2011**, *385*, 195–200. [\[CrossRef\]](#)
59. Bao, Y.; Guo, H.; Jiang, L.; Liu, Z.; Qu, J.; Zhang, C.; Jia, X.; Chen, K. Heterostructured WO<sub>3</sub>/RGO/protonated g-C<sub>3</sub>N<sub>4</sub> three-layer nanosheets for enhanced visible-light photocatalytic activity. *Appl. Surf. Sci.* **2019**, *496*, 143639. [\[CrossRef\]](#)
60. Raza, W.; Ahmad, K.; Alharethy, F.; Kim, H. Designing of Ag decorated ZnO catalyst for on-demand and sustainable H<sub>2</sub> production at room temperature. *Colloids Surf. A Physicochem. Eng. Asp.* **2023**, *673*, 131757. [\[CrossRef\]](#)
61. Raza, W.; Faisal, S.M.; Owais, M.; Bahnemann, D.; Muneer, M. Facile fabrication of highly efficient modified ZnO photocatalyst with enhanced photocatalytic, antibacterial and anticancer activity. *RSC Adv.* **2016**, *6*, 78335–78350. [\[CrossRef\]](#)
62. Kurnia, F.; Ng, Y.H.; Amal, R.; Valanoor, N.; Hart, J.N. Defect engineering of ZnS thin films for photoelectrochemical water-splitting under visible light. *Sol. Energy Mater. Sol. Cells* **2016**, *153*, 179–185. [\[CrossRef\]](#)
63. Raza, W.; Tesler, A.B.; Mazare, A.; Tomanec, O.; Kment, S.; Schmuki, P. Pt Single Atoms as Co-Catalysts on CdS-Sensitized Single-Crystalline TiO<sub>2</sub> Nanoflakes for Enhanced Visible Light Photocatalytic H<sub>2</sub> Generation. *ChemCatChem* **2023**, *15*, e202300327. [\[CrossRef\]](#)
64. Osuagwu, B.; Raza, W.; Tesler, A.B.; Schmuki, P. Facile Approach of Direct Sulfidation of FTO to Form Vertically Aligned SnS<sub>2</sub> Nanoflake Photoanodes for Efficient Photoelectrochemical Water Splitting. *ACS Appl. Energy Mater.* **2021**, *4*, 8395–8400. [\[CrossRef\]](#)
65. Raza, W.; Tesler, A.B.; Mazare, A.; Schmuki, P. Solar Light-Induced Photoelectrochemical H<sub>2</sub> Generation Over Hierarchical TiO<sub>2</sub> Nanotube Arrays Decorated with CdS Nanoparticles. *J. Electrochem. Soc.* **2024**, *171*, 066506. [\[CrossRef\]](#)
66. Puentes-Prado, E.; Garcia, C.R.; Oliva, J.; Galindo, R.; Bernal-Alvarado, J.J.; Diaz-Torres, L.A.; Gomez-Solis, C. Enhancing the solar photocatalytic hydrogen generation of ZnS films by UV radiation treatment. *Int. J. Hydrogen Energy* **2020**, *45*, 12308–12317. [\[CrossRef\]](#)
67. Yao, Z.; Hou, X.; He, Y.; Li, D.; Jiang, Z. Hydrothermal synthesis of Ni-doped ZnS solid solution photocatalysts for photocatalytic H<sub>2</sub> production. *Res. Chem. Intermed.* **2019**, *45*, 4927–4940. [\[CrossRef\]](#)
68. Tie, L.; Sun, R.; Jiang, H.; Liu, Y.; Xia, Y.; Li, Y.-Y.; Chen, H.; Yu, C.; Dong, S.; Sun, J.; et al. Facile fabrication of N-doped ZnS nanomaterials for efficient photocatalytic performance of organic pollutant removal and H<sub>2</sub> production. *J. Alloys Compd.* **2019**, *807*, 151670. [\[CrossRef\]](#)
69. Ren, H.; Ye, K.; Chen, H.; Wang, F.; Hu, Y.; Shi, Q.; Yu, H.; Lv, R.; Chen, M. ZnO@ZnS core-shell nanorods with homologous heterogeneous interface to enhance photocatalytic hydrogen production. *Colloids Surf. A Physicochem. Eng. Asp.* **2022**, *652*, 129844. [\[CrossRef\]](#)
70. Bolatov, A.; Manjovel, A.; Chouchene, B.; Balan, L.; Gries, T.; Medjahdi, G.; Uralbekov, B.; Schneider, R. Ternary ZnS/ZnO/Graphitic Carbon Nitride Heterojunction for Photocatalytic Hydrogen Production. *Materials* **2024**, *17*, 4877. [\[CrossRef\]](#)

**Disclaimer/Publisher's Note:** The statements, opinions and data contained in all publications are solely those of the individual author(s) and contributor(s) and not of MDPI and/or the editor(s). MDPI and/or the editor(s) disclaim responsibility for any injury to people or property resulting from any ideas, methods, instructions or products referred to in the content.